Preparation and Characterization of Non-Aromatic Ether Self-Assemblies on a HOPG Surface

Jasna Alić,[a] Ivana Biljan,[b,*] Zoran Štefanić,[c] Marina Šekutor[a,*]

[a] *Department of Organic Chemistry and Biochemistry, Ruđer Bošković Institute, Bijenička 54, 10 000 Zagreb, Croatia,* msekutor@irb.hr

[b] *Department of Chemistry, Faculty of Science, University of Zagreb, Horvatovac 102a, 10 000 Zagreb, Croatia,* ibiljan@chem.pmf.hr

[c] *Department of Physical Chemistry, Ruđer Bošković Institute, Bijenička 54, 10 000 Zagreb, Croatia*

Keywords: diamondoids, London dispersion interactions, highly oriented pyrolytic graphite (HOPG), ethers, monolayers

Abstract

On-surface self-assemblies of aromatic organic molecules have been widely investigated, but the characterization of analogous self-assemblies consisting of fully sp^3-hybridized molecules remains challenging. The possible on-surface orientations of alkyl molecules not exclusively comprised of long alkyl chains are difficult to distinguish because of their inherently low symmetry and non-planar nature. Here, we present a detailed study of diamondoid ethers, structurally rigid and fully saturated molecules, which form uniform 2D monolayers on a highly oriented pyrolytic graphite (HOPG) surface. Using scanning tunneling microscopy (STM), various computational tools, and X-ray structural analysis, we identified the most favorable on-surface orientations of these rigid ethers and accounted for the forces driving the self-organization process. The influence of the oxygen atom and London dispersion interactions were found to be responsible for the formation of the observed highly ordered 2D ether assemblies. Our findings provide insight into the on-surface properties and behavior of non-aromatic organic compounds and broaden our understanding of the phenomena characteristic of monolayers consisting of non-planar molecules.

Introduction

In the ever-changing world there is an ongoing need for new and sustainable materials. Present and future technologies will therefore most certainly benefit from further development

of carbon-based materials. From different existing allotropic modifications of carbon, diamond is an especially attractive scaffold for nanomaterial design due to its high thermodynamic stability, despite possessing drawbacks that include uncontrollable variations in thickness after monolayer formation and limited ability for selective chemical functionalization.[1] An alternative to nanodiamond particles are diamondoids,[2, 3] naturally occurring sp^3-hybridized cage hydrocarbons available from oil sources[4] that include the best of both worlds, retaining the diamond-like structure while enabling chemical functionalization. The advantage of using diamondoids in the design of new functional materials lies in the bottom-up principle, meaning that one can control layer formation and properties by first controlling the chemical properties and group functionalization of individual molecules that then build up the desired self-assembly. Moreover, due to structural similarity of their cage backbones to the diamond crystal lattice, diamondoid derivatives have a potential to bridge the gap between flexible organic molecules and bulk diamond. In recent years advances in selective chemical functionalization of diamondoid C–H bonds[5] resulted in their application in the design of new ordered materials since strictly defined substitution patterns are crucial for achieving reproducible electronic properties.[2, 3, 6-9] In order to advance the field of advanced organic materials based on bulky, sp^3-hybridized molecules, the ongoing challenge is to prepare novel functional scaffolds capable of controlled on-surface self-assembly.

It should be noted that until now great focus has been on the on-surface behavior of mainly aromatic molecules, with a popular tool for analyzing surface phenomena being scanning tunneling microscopy (STM) and atomic force microscopy (AFM).[10-16] However, significantly fewer examples exist that describe adsorptive on-surface behavior of saturated organic compounds, and the ones that do focus mostly on derivatives with long alkyl chains present in the structure.[17-23] That is not surprising since for the assembly characterization aromatics possess several advantages over many saturated molecules: they are able to easily adsorb on a surface in a straightforward manner due to their planar structure, they are rich in electrons and their aromatic ring are suitable for facile detection using spectroscopy and their on-surface behavior can often be predicted based solely on the interactions of functional groups present in their structure. On the other hand, identification of non-aromatic compounds deposited on surfaces is made difficult with inherent problems caused by their chemical nature: the bulkiness and unevenness of the structure enables a plethora of possible on-surface adsorption patterns that are hard to characterize and difficult to unequivocally assign. Aside from the mentioned compounds with alkyl chains, characterization of self-assemblies

consisting of purely aliphatic molecules is still a challenge. However, it should be noted that quite recently several on-surface STM and/or AFM studies of adsorbed diamondoids emerged, the notable examples being self-assembly of adamantane[24] and tetramantane[25-28] and diamondoid thiol[29, 30] molecules on metal surfaces.

From a practical perspective, it is also important to mention that functionalized diamondoids display negative electron affinities (NEA) which makes them good monochromatic electron emitters,[7, 31-34] the phenomena being a consequence of electron pile-up at the band minimum (LUMO) occurring before the emission process from the on-surface monolayers. Different heteroatoms present in the diamondoid cage scaffold can tune the molecular optical gap, essentially the HOMO-LUMO difference, and thus determine the nature of the emission spectrum.[32] What is more, use of bigger functionalized diamondoids enhances emission properties due to increased physico-chemical stabilization provided by the diamondoid cage framework.[35] However, up to now only diamondoid derivatives that terminated with heteroatom groups or had a heteroatom incorporated into the cage itself[36-38] were studied in the context of nanomaterial applicability and no expanded scaffolds combining two or more diamondoid cages connected with heteroatoms were considered. We therefore focused our attention on preparing exactly such unexplored scaffolds with potential future application as anchoring subunits in diverse fields of nanotechnology. As a first compound class to study we focused on ethers. Diamondoid ether derivatives comprised of two directly connected cage moieties *via* an oxygen atom are virtually unknown, the only example in the literature to the best of our knowledge being a simple 1,1'-diadamantyl ether (**1**).[39-44] This compound was first isolated as a low yielding side-product of different coupling reactions and was only recently prepared in a targeted synthetic effort.[45] Up to now, studies of its properties included spectroscopic characterization of its complexes formed with different solvent molecules and evaluation of the importance of London dispersion interactions[46] acting in such supramolecular systems.[45, 47] Exploration of on-surface assemblies and capability of monolayer formation for ether **1** and similar diamondoid ethers remains unexplored to date and was thus the focus of our interest.

Results and Discussion

In the scope of this study we prepared the homocoupled ether **1** and heterocoupled diamondoid ethers **3** and **4** that were comprised of one adamantyl and one diamantyl subunit, substituted in either the apical or the medial position of the diamantane cage, respectively

(Figure 1). Model *tert*-butyl substituted ether **2** was also prepared in order to evaluate the difference in self-assembly properties when the ether scaffold is comprised from a combination of a cage and a branched hydrocarbon substituent and not solely from two diamondoid subunits.

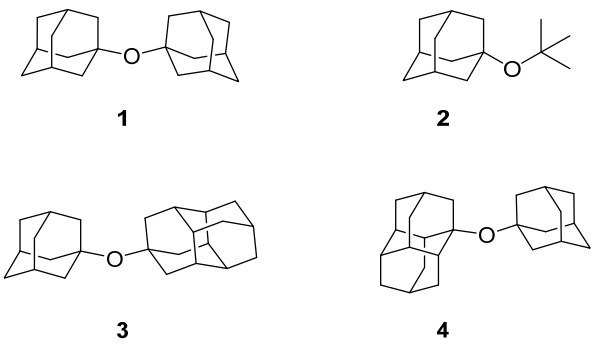

Figure 1. Structures of the prepared diamondoid ethers **1**–**4**.

Diamondoid ethers **1**–**4** were prepared by condensing the corresponding alcohol[5] with diamondoid methanesulfonates[48] in the presence of the TEA base, a procedure similar to the one previously reported for preparation of 1,1'-diadamantyl ether (**1**).[45] Target compounds were obtained in good yields and high purity needed for deposition on a highly oriented pyrolytic graphite (HOPG) surface. To enable the investigation of the on-surface self-assembly of diamondoid ethers **1**–**4** under ambient conditions**,** STM experiments were conducted at 1-octanol/HOPG interface. In general, STM imaging at the liquid/solid interface proved to be an excellent approach for studying the structural features of physisorbed self-assembled monolayers at the molecular level.[49, 50] Numerous literature examples describe assemblies on a HOPG surface but they typically deal with aromatic compounds [51-55] and/or derivatives with long alkyl chains. [56-64] However, the novelty of our approach lies in the combination of STM imaging with detailed computations suited for structural analysis beyond solely aromatic scaffolds, thus enabling reliable on-surface characterization of purely aliphatic molecules which possess no additional alkyl chain moieties. All STM images in the current work were acquired in the constant-height mode, meaning that the image contrast corresponds to the changes in tunneling current at constant bias voltage (white represent the highest and black the lowest tunneling current). As revealed by high-resolution STM images (Figure 2a-c), deposition of a droplet of the ether solution in 1-octanol on freshly cleaved HOPG surface results in the formation of a well-defined monolayer. It should be noted that the acquired STM images confirmed the spontaneous self-assembly phenomena for ethers **1**–

3, while less symmetrical ether **4** with a medially substituted diamantane subunit failed to produce on-surface monolayers.

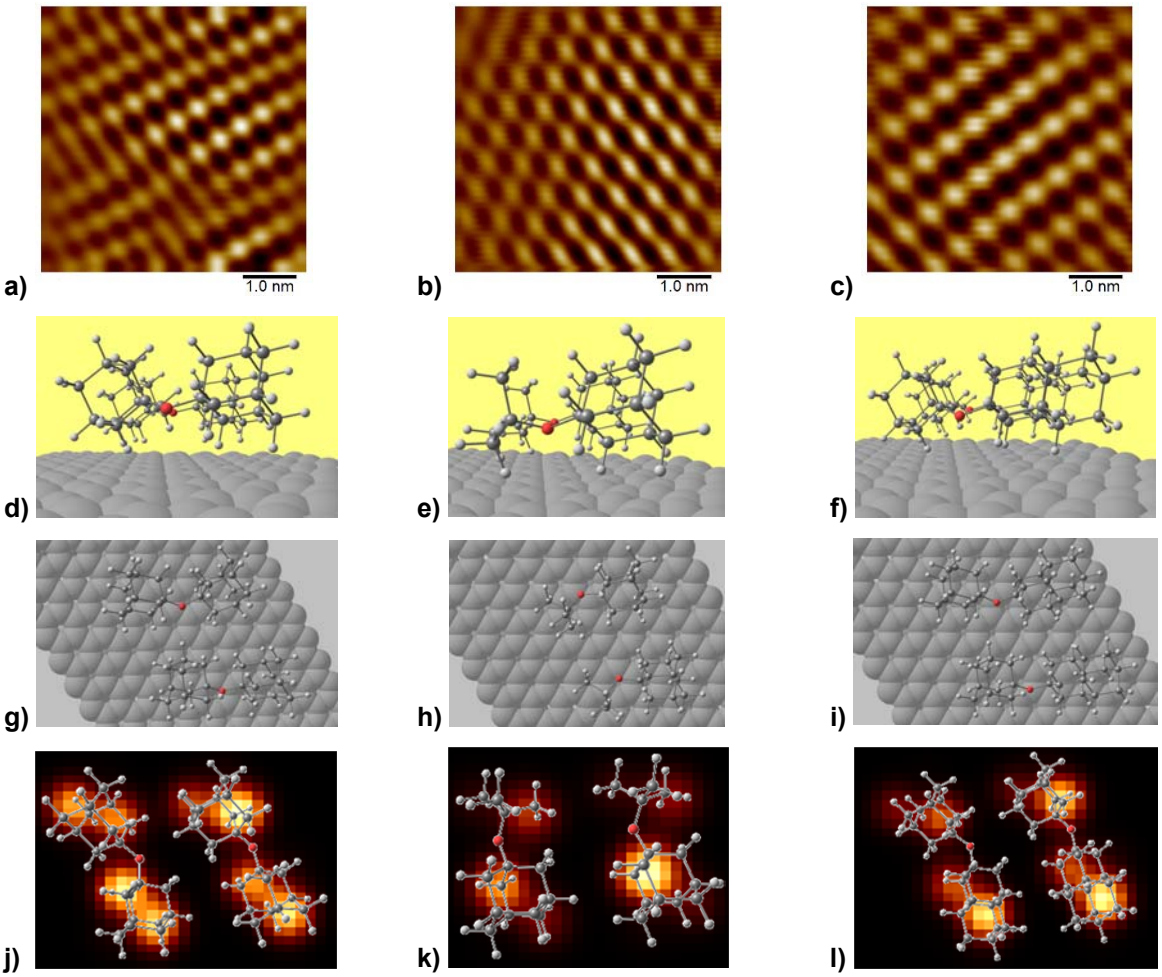

Figure 2. On-surface characterization of ethers **1**–**3**. Constant-height STM images (scan size 5 nm × 5 nm) depicting self-assembly on the HOPG surface of ethers **1** (a), **2** (b) and **3** (c), the computed on-surface structures of **11** (d, g), **22** (e, h) and **33** (f, i) corresponding to the observed structural motifs, and simulated constant-height STM images overlapped with structures for **11** (j), **22** (k) and **33** (l) constructed from electron densities obtained by computations at the B3LYP-D3(BJ)/def2-TZVPP level of theory.

As can be observed from the collected STM images of the ether monolayers on the HOPG surface, all three compounds form a consistent 2D lattice but the underlying characteristics of the respective self-organized network are different. Namely, the bisadamantyl ether **1** forms a uniform, rectangle-like pattern on the HOPG surface while the *tert*-butyl analogue **2** displays arrangement characteristics more akin to a parallelogram (see Figures 2a and b). This observation suggests that a molecule with a higher overall symmetry has a tendency to

translate that molecular symmetry to a more highly symmetric self-assembled layer and demonstrates that initial geometrical properties of used diamondoid molecules have a significant impact on the emerging spatial arrangement of the ensembles. Furthermore, note that the mixed ether **3** again shows an on-surface self-assembly pattern similar to the one found for ether **1** (Figure 2c). This observation can be explained by similar symmetry of the two since the apically substituted diamantane cage present in the structure of **3** can in this case be viewed as essentially an elongation of the adamantane cage in the direction of the ether C–O–C bond. Additionally, when applying the same reasoning to the medially substituted ether **4**, the molecular symmetry argument indeed also explains our finding that **4** does not form 2D monolayers on HOPG under these reaction conditions, since that structure is significantly less rod-shaped and the molecules can arrange in many different orientations on a surface that are sufficiently stable.

It should be noted that the studied ether molecules are only adsorbed on the surface with no covalent bond formation occurring. The interactions between them are expected to be governed by London dispersion attraction since they do not possess other functional groups besides the ether group (no possibility for *e.g.*, strong hydrogen bonding) and since diamondoid cages are known to be good dispersion energy donors. Consequently, the self-assembly is expected to be driven by two influences: the interaction with the graphite surface and the intermolecular interactions between the ether molecules themselves. Here a question also arises whether the electronegative oxygen atoms play a significant part in the adsorption of the ether to the surface or are they more engaged in interactions with neighboring molecules. Therefore, to gain more insight into the monolayer formation process and the underlying influence of dispersion on it and to fully characterize the obtained STM images, we turned to computational tools. We used the semi-empirical quantum mechanical GFN2-xTB method[65, 66] to obtain the energy profiles of the explored ether molecules when deposited on a graphite surface. A similar approach was recently successfully applied in studies of on-surface behavior of some other diamondoids.[30, 67] Geometry optimization of ether molecules on the graphite surface consisting of two layers of 400 carbon atoms in total afforded different possible molecular orientations (Figure 3) that showcased different interaction energies (Table 1). Here again it should be underlined that the overall interaction energy of such self-assemblies that we obtain through computational means also consists of two main contributions: interaction of ether molecules with the underlying graphite surface and intermolecular interaction between the individual ethers facilitated by many close contacts existing between the molecules. First the optimized geometries of individual ether

molecules were obtained by using the B3LYP-D3(BJ)/def2-TZVPP level of theory and then used as initial geometries for the generation of starting on-surface assemblies that subsequently underwent the GFN2-xTB optimization. Note that Grimme's D3 correction[68-70] was applied in all DFT computations since dispersion interactions comprise a significant energetic contribution to the stabilization of sp^3-hybridized bulky molecules like diamondoids.[27, 28, 46, 71, 72]

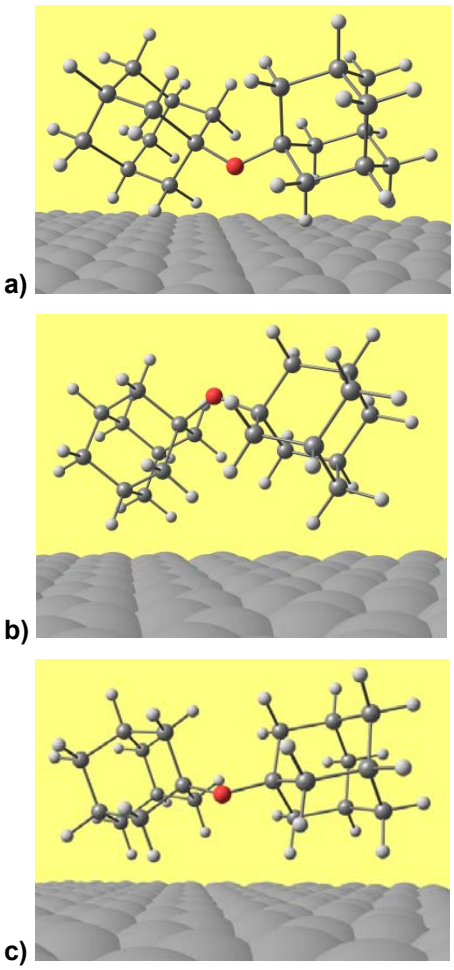

Figure 3. Feasible on-surface orientations of ether **1** on graphite. Functional group directed, **a** – towards the surface, **b** – away from the surface, and **c** – parallel to the surface.

Performed on-surface geometry optimization revealed three primary molecular orientations of these ethers on graphite that we denominated as **a**, **b** and **c**, respectively (Figure 3). Orientation **a** is characterized by the ether oxygen atom pointing towards the surface while in orientation **b** it faces away from the surface. In contrast, orientation **c** has the oxygen arranging parallel to the surface, making it available for intermolecular side interactions. Analysis of the binding energy shows that orientations **a** and **c** are more favorable than

orientation **b**, which illustrates the importance of the oxygen for the deposition process. Namely, interaction of the ether group and its free electron pairs with either the graphite rings (in **a**) or with the neighboring C–H groups (in **c**) facilitates stronger binding when compared to the binding capability of the sole cage subunits (in **b**). Moreover, increase in the size of the dispersion energy donor substituent in symmetrically similar structures results in better energetic stabilization; the energetic release for the most stable respective orientation is higher for the bisadamantyl ether **1** than for the *tert*-butyl substituted analogue **2** (Table 1). Energetics obtained for ether **3** further showcase this stabilization trend. These findings have implications for computation-assisted predicting of the self-organization probability of a given structure and therefore can aid in future design of feasible monolayer generating molecules, where a synergy between structural features and a favorable energetic profile is a must.

Note that the overall binding energy increases non-linearly when another ether molecule is included in the assembled structure in such a way that it can freely interact with the first ether molecule present. Thus, larger overall energy difference values were obtained than it would be the case for simply adding up the energy differences for two non-interacting molecules placed on a surface (see Table 1). This confirms the importance of side interactions acting between neighboring ether molecules in driving the directed on-surface assembly forward. The described feature has important general implications for assessing the molecule-to-molecule and molecule-to-material interface attraction for this type of systems. Namely, it is known that a fine interplay exists between side and surface interactions during the self-assembly processes,[73] especially when the substrate is relatively weakly binding, as is the case for HOPG. We quantified computationally that the interactions between diamondoid ethers and the HOPG substrate (adsorption energies) are indeed stronger than the interaction between two molecules on the surface (2D monolayer energies), but crucial to note is that the molecule-to-molecule side attraction is actually the main driving force for the fine-tuned formation of an ordered 2D assembly. What is more, the strength of side interactions can even change the preferred ether orientation from the initial one present immediately after deposition to the one adopted after the introduction of more molecules. For example, this appears to be the case for ether **1** that tilts upon self-assembly from a surface-directed orientation **a** towards a more side-directed orientation **c**. Such rotation of molecules on surfaces was already observed for bulky molecules[28] and comes as no surprise since dispersion is additive in nature and thrives best when many suitable molecule regions are in close contact with one another. Despite the inherent non-directionality of dispersion

interactions, behavior of bulky diamondoid ethers on the graphite surface still follows a somewhat predictable pattern, as it seems that the oxygen atom directs the initial point of molecular attraction while the C–H bond rich bulky regions then strengthen the emerging non-covalent supramolecular binding and thus finalize the on-surface 2D lattice formation.

Table 1. Computed interaction energies (ΔE) of diamondoid ether orientations on the graphite surface in kcal mol^{-1}.[a]

Diamondoid ether	Orientation on surface	ΔE / kcal mol^{-1} (one molecule)	ΔE / kcal mol^{-1} (two molecules)
1	**a**	–10.6	–24.0
	b	–8.0	–18.9
	c	**–11.8**	**–25.4**
2	**a**	–9.0	–20.0
	b	–8.3	–18.1
	c	**–9.9**	**–20.3**
3	**a**	–11.8	–27.2
	b	–11.3	–20.6
	c	**–12.7**	**–28.2**
4	**a**	–10.3	–22.1
	b	–8.1	–23.3
	c	**–10.9**	**–23.6**

[a] Interaction energies are defined as the energy difference between the on-surface assembly and the corresponding number of molecules and the lone graphite slab (a two layered C_{400} cut-out).

Having obtained insights into favorable orientations of studied ether molecules on the HOPG surface, we can now go back to our experimental observations and complete the structural analysis of the monolayers. Since we determined that the on-surface orientation **c** is the most favorable for this series of compounds, we made a comparison between the measured and the computed data. As can be seen in Figure 2, there is an excellent fit between the observed STM images and the computed molecular orientations, noting that the energetically most favorable modelled assemblies **c** (two molecules of the respective ether, *i.e.*, **11**, **22** and **33**, Figure 2d-1) show a striking visual resemblance to the observed on-surface pattern of the monolayers (Figure 2a-c). Such a good match is not only visual but can be expressed quantitatively as well, for example, for ether **1** the measured lengths of the rectangle-like pattern amount to 0.74 ± 0.03 and 1.03 ± 0.05 nm, respectively, while the corresponding distances in the computed structure amount to 0.75 and 1.00 nm, respectively. Similar comparisons can be

made between other STM images and the corresponding computed on-surface structures as well. However, taking into account that the STM technique actually visualizes electron densities of the molecules, we also performed electron density distribution computations using the B3LYP-D3(BJ)/def2-TZVPP level of theory on the assembly geometries **c** optimized by the GFN2-xTB approach. From the computed electron densities we then constructed simulated STM images (Figure 2j-l) and the emerging matching pattern additionally supports the proposed on-surface arrangement of diamondoid ether molecules on HOPG. We also performed electron density computation for ether **4** and found that the simulated STM image of the theoretical assembly **44** provides a somewhat less symmetric density pattern, which is in line with the experiment, since **4**, as already mentioned, does not self-assemble on HOPG under these conditions. Additional comparison of the recorded STM data with the computed electron density distribution in ether molecules is illustrated in Figure 4 where a 3D STM image of **33** is depicted alongside the corresponding electron density distribution. Again, one can observe the close similarity between the experimental data and the computational model, giving credence to the approach used for the analysis of the diamondoid ether self-assemblies and for predicting their monolayer formation capability.

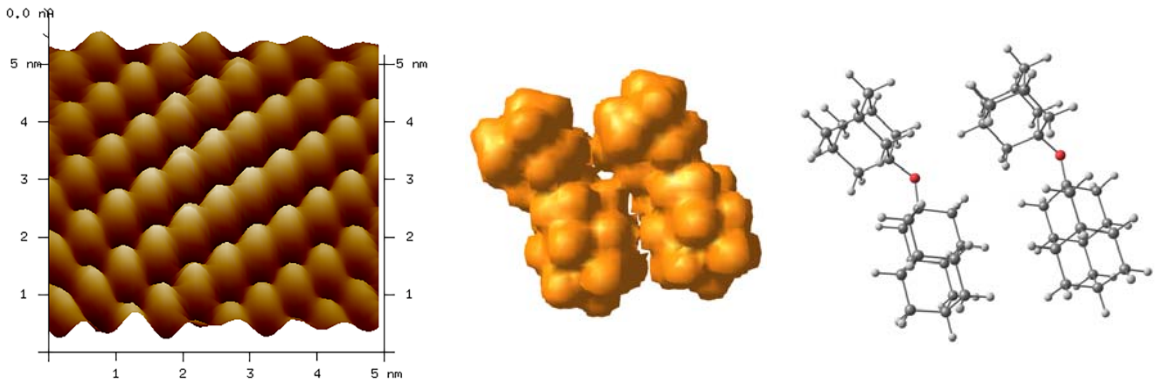

Figure 4. Comparison of a 3D STM image of ether **3** deposited on a HOPG surface with ether electron density distribution of **33** obtained by computations using the B3LYP-D3(BJ)/def2-TZVPP level of theory.

Furthermore, to better visualize the regions in the ether molecules where dispersion interactions prevalently take place, we generated the corresponding NCI plots for self-assembled structures in the most stable orientation **c** (Figure S11). As expected, these interacting regions are most prevalent on the sides of the ether molecules where they can engage in close contacts with analogous C–H rich areas of the neighboring molecules and in

that manner drive the supramolecular assembly process forward. For example, in assembly **33** depicted in Figure 5 the regions favorable for intermolecular interaction are the molecule sides running in parallel to the central C–O–C, while the region best suited for intramolecular interaction in the ether is the area between the two cage subunits of the molecule.

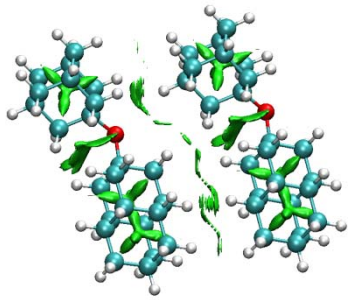

33 – top view

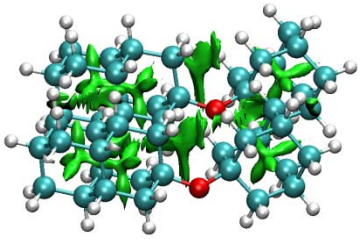

33 – side view

Figure 5. NCI plots of self-assembled structure **33** positioned in orientation **c**. Non-covalent interactions are depicted in green.

Lastly, going one step further in our evaluation of the importance of dispersion interactions for self-organization of bulky diamondoid ethers, we performed X-ray analysis of the crystalline forms of ethers **1–4**. Up to now we focused on the formation of a uniform 2D structural network on a surface but crystallization gave us access to a 3D ordered system as well. Even though the dimensionality of these assemblies differs, the main driving forces remain the same and the arrangement of ether molecules in a crystal lattice can be very informative in regards to the quantification of the distances for typical intermolecular close contacts. Depicted in Figure 6 are the 3D packings of derivatives **1** and **4** and, as is expected, the bulky cages now interact with each other in all three directions, since no flat surface is present to restrain them. Note that while molecules of ether **1** can still pack much more tightly than those of **4** in a 3D space, the possibility to assemble in another direction suffices for achieving the ordered arrangement of **4** in the form of a crystal periodicity. As the energetic stabilization through dispersion grows with more close contacts between the cages, so the molecules “click together” more readily and the uniform 3D spatial arrangement becomes

possible, unlike the 2D arrangement on a surface that appears to be irregular and could not be detected by imaging. Similar packing trends were also found in the crystal structures of **2** and **3** (Figure S3).

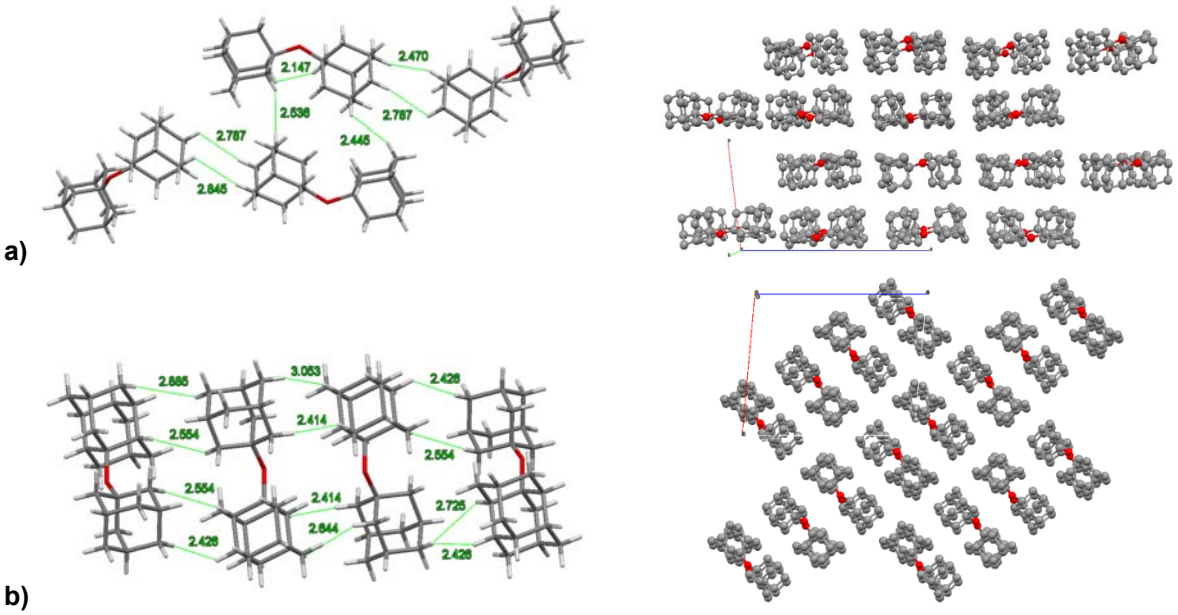

Figure 6. Packing of molecules obtained from the X-ray crystal structures of a) compound **1**, space group *P* 2/*c*, b) compound **4**, space group *P 2/n*. The crystal packing in both structures is dominated by dispersion interactions between the cages. Selected close intermolecular contacts are depicted as green dashed lines with the corresponding distances in Å. Grey (carbon), white (hydrogen), red (oxygen).

To summarize, combined experimental and theoretical findings we presented herein are a step forward in understanding the forces acting on non-aromatic molecules that spontaneously assemble on surfaces like HOPG. Moreover, diamondoid ethers appear to be a promising scaffold for on-surface anchoring and provide uniform monolayers on a HOPG surface and potentially beyond, with further structural modification of such compounds possibly resulting in functional materials applicable in the surface coating manufacture.

Conclusions

In the scope of this study we characterized self-assembled monolayers consisting of diamondoid ethers using experimental and computational tools. The STM technique provided us with the images of the formed 2D ether assemblies while the conducted geometry

optimizations revealed the most stable on-surface orientations of molecules under study. The experimental constant-height images were compared with the simulated ones obtained from electron density computations and were a good match, giving credence to our computational approach. We also confirmed that the oxygen atom influence combined with dispersion interactions play a crucial role in the on-surface organization of the studied ethers, a finding additionally backed up by the constructed NCI plots. Lastly, we also compared the spatial 2D *vs.* 3D organization of diamondoid ethers and identified numerous close contacts in both instances, further pointing to the role of dispersion in the formation of periodic structures for this class of fully sp^3-hybridized compounds. Our findings pave the way for future investigations of on-surface behavior of complex non-aromatic molecules and further studies dealing with the influence of a heteroatom on the self-organization process are already under way.

Experimental

Materials and Methods: All ^{1}H and ^{13}C NMR spectra were recorded with Bruker AV-300 or AV-600 NMR spectrometers and the NMR spectra were referenced to the residual proton or carbon signal of the used deuterated solvent as an internal standard. IR spectra were recorded with a FT-IR ABB Bomem MB 102 or FT IR-ATR PerkinElmer UATR Two spectrometers (range 400 to 4000 cm^{-1}). MALDI-TOF MS spectra were obtained in "reflectron" mode with an Applied Biosystems Voyager DE STR instrument (Foster City, CA). GC-MS analyses were performed on an Agilent 7890B/5977B GC/MSD instrument equipped with a HP-5ms column. Determination of melting points was performed by using an Original Kofler Mikroheitztisch apparatus (Reichert, Wien) or by differential scanning calorimetry (DSC) analysis using Simultaneous Thermal Analyzer (STA) 6000 (PerkinElmer, Inc.) in a platinum crucible with cap (non-hermetically sealed). Around 5 mg of each sample was analyzed using a 10°C/min heating rate and under 20 mL/min nitrogen gas flow. Data was processed in Pyris Data Analysis software. All the solvents were obtained from commercial sources and used without further purification. 1,1'-Diadamantyl ether (**1**) was prepared according to a previously published procedure.[45]

General procedure for diamondoid ether synthesis: The corresponding diamondoid methanesulfonate (1 equivalent), the corresponding alcohol (1 equivalent) and TEA (1.2 – 1.5 equivalent) were heated in an autoclave at 100 °C for 24 h. The reaction mixture was dissolved in CH_2Cl_2, washed with water, 5% H_2SO_4 and $NaHCO_3$ (sat., aq.). The organic

phase was dried over Na_2SO_4, filtered and evaporated. The resulting crude product was purified using column chromatography (Al_2O_3 or SiO_2) and the corresponding diamondoid ether was isolated as a white solid.

1-Adamantyl-*tert*-butyl ether (**2**).[74] A round-bottom flask (50 ml) was filled with 1-adamantyl methanesulfonate (**6**) (2.30 g, 10 mmol), *tert*-butanol (10 ml, 105 mmol) and TEA (1.60 ml, 11.5 mmol) and the reaction mixture was heated under reflux for 24 h under a nitrogen atmosphere. The reaction mixture was dissolved in CH_2Cl_2 and washed with H_2O (2 x 20 ml), the organic layer was dried over Na_2SO_4 and the solvent was removed on a rotary evaporator. The crude mixture was purified by column chromatography (Al_2O_3, activity V, *n*-hexane), yielding **2** (1.75 g, 85%) as white solid. M.p. 55–57 °C. ^{1}H NMR (300 MHz, $CDCl_3$), δ/ppm: 2.09 (br s, 3H), 1.92-1.82 (m, 6H), 1.65-1.55 (m, 6H), 1.29 (s, 9H). ^{13}C NMR (75 MHz, $CDCl_3$), δ/ppm: 74.1 (1C), 73.9 (1C), 45.3 (3C), 36.5 (3C), 32.2 (3C), 31.0 (3C). IR (KBr), ν_{max}/cm^{-1}: 2973 (m), 2908 (s), 2852 (m), 1453 (w), 1360 (m), 1233 (w), 1194 (m), 1116 (m), 1087 (s), 997 (m). MS (EI), *m*/*z*: 208.2 (M^+).

1-Adamantyl-4-diamantyl ether (**3**). According to the general procedure for the synthesis of diamondoid ethers, 4-diamantyl methanesulfonate (0.150 g, 0.53 mmol), adamantan-1-ol (0.081 g, 0.53 mmol) and TEA (0.112 ml, 0.80 mmol) were heated in an autoclave at 100 °C for 24 h. According to the GC-MS analysis of the resulting reaction mixture, 1-adamantyl-4-diamantyl ether (**3**) was the major product of the reaction (58%) while 4,4'-didiamantyl ether (**5**) was a side product (15%). The crude reaction mixture was chromatographed on a silica gel column using *n*-hexane as eluent and afforded a mixture of ethers **3** and **5**. After repeated recrystallization from diethyl ether pure products **3** (0.093 g, 52%) and **5** (0.018 g, 10%) were obtained, both as white solids. 1-Adamantyl-4-diamantyl ether (**3**): M.p. 263–265 °C. ^{1}H NMR ($CDCl_3$, 300 MHz), δ/ppm: 2.08 (br. s, 3H), 1.89-1.84 (m, 15H), 1.78-1.74 (m, 1H), 1.72-1.68 (m, 9H), 1.60-1.57 (m, 6H). ^{13}C NMR ($CDCl_3$, 150 MHz), δ/ppm: 74.2 (1C), 73.4 (1C), 46.2 (3C), 45.8 (3C), 40.1 (3C), 37.3 (3C), 36.6 (3C), 36.5 (3C), 31.1 (3C), 25.7 (1C). IR (neat), ν_{max}/cm^{-1}: 2871 (s), 2847 (m), 1439 (w), 1342 (m), 1248 (w), 1110 (m), 1098 (s), 1086 (m), 1033 (m), 953 (w), 877 (w), 798 (w). MS (EI), *m*/*z*: 338.3 (M^+). HRMS (MALDI): calcd. for $[C_{24}H_{34}ONa]^+$ 361.2507; found 361.2510. 4,4'-Didiamantyl ether (**5**): M.p. 221–223 °C. ^{1}H NMR ($CDCl_3$, 600 MHz), δ/ppm: 1.90-1.85 (m, 18H), 1.78-1.75 (m, 2H), 1.71-1.69 (m, 18H). ^{13}C NMR ($CDCl_3$, 150 MHz), δ/ppm: 73.4 (2C), 46.1 (6C), 40.1 (6C), 37.3 (6C), 36.6 (6C), 25.7 (2C). IR (neat), ν_{max}/cm^{-1}: 2888 (s), 2869 (s), 2847 (s), 1103 (s), 1049 (m), 925 (w). MS (EI), *m*/*z*: 390.3 (M^+). HRMS (MALDI): calcd. for $[C_{28}H_{38}O]^+$ 390.2923; found 390.2920.

1-Adamantyl-1-diamantyl ether (**4**). According to the general procedure for the synthesis of diamondoid ethers, 1-adamantyl methanesulfonate (**6**) (0.230 g, 1 mmol), diamantan-1-ol (0.204 g, 1 mmol) and TEA (0.21 ml, 1.5 mmol) were heated in an autoclave at 100°C for 24 h. Purification by column chromatography on Al_2O_3 (activity V, *n*-hexane as eluent) gave the pure product **4** (0.200 g, 59%) as a white solid. M.p. 147–149 °C. ^{1}H NMR ($CDCl_3$, 600 MHz), δ/ppm: 2.33 (d, J = 12.1 Hz, 2H), 2.07 (br. s, 3H), 2.05-2.02 (m, 1H), 1.96-1.93 (m, 2H), 1.92-1.90 (m, 6H), 1.89 (br. s, 2H), 1.82 (br. s, 2H), 1.71-1.67 (m, 1H), 1.65-1.55 (m, 13H), 1.30 (d, J = 12.1 Hz, 2H). ^{13}C NMR ($CDCl_3$, 150 MHz), δ/ppm: 76.9 (1C), 74.1 (1C), 45.6 (1C), 45.5 (3C), 43.7 (2C), 40.3 (2C), 38.5 (1C), 37.7 (2C), 36.8 (1C), 36.6 (3C), 33.0 (2C), 31.1 (3C), 30.5 (1C), 25.7 (1C). IR (neat), ν_{max}/cm^{-1}: 2874 (m), 2845 (m), 1454 (w), 1343 (m), 1300 (w), 1099 (s), 1075 (m), 1025 (m), 951 (w), 903 (w), 818 (w). MS (EI), *m*/*z*: 338.3 (M^+). HRMS (MALDI): calcd. for $[C_{24}H_{34}ONa]^+$ 361.2507; found 361.2493.

General procedure for the synthesis of diamondoid methanesulfonates: In a 25 mL round-bottom flask, the corresponding alcohol (1 equivalent), TEA (3.5 equivalent) and dry CH_2Cl_2 (5 ml) were added and cooled with an ice bath. A solution of methanesulfonic anhydride (1.5 equivalent) in cold CH_2Cl_2 (2 ml) was added dropwise with vigorous stirring. Upon addition, the resulting pale yellow solution was stirred for additional 10 min at 0 °C and then for 20-30 min at room temperature. The reaction mixture was diluted with CH_2Cl_2 (5 ml) and washed with cold 5% H_2SO_4 (5 ml) and $NaHCO_3$ (sat., aq., 10 ml), followed by drying of the organic phase over Na_2SO_4. The solvent was evaporated to obtain the crude white product which was used in the next step without further purification.

1-Adamantyl methanesulfonate (**6**).[48] By following the general procedure for the synthesis of diamondoid methanesulfonates, adamantan-1-ol (0.76 g, 5 mmol), TEA (2.4 ml, 17.5 mmol) and CH_2Cl_2 (20 mL) were cooled to 0 °C. A solution of methanesulfonic anhydride (1.3 g, 7.5 mmol) in cold CH_2Cl_2 (5 ml) was added dropwise and the reaction mixture was stirred for 10 min at 0 °C and then for 20 min at room temperature. Upon completion of the reaction, the mixture was treated according to the general procedure to yield product **6** almost quantitatively. The recorded NMR spectra of **6** correspond to the ones that have been previously reported.[45]

4-Diamantyl methanesulfonate (**7**). By following the general procedure for the synthesis of diamondoid methanesulfonates, diamantan-4-ol (0.20 g, 1 mmol) was dissolved in dry CH_2Cl_2 (5 ml) and TEA (0.5 ml, 3.5 mmol) was added. The reaction mixture was cooled to 0 °C, a solution of methanesulfonic anhydride (0.26 g, 1.5 mmol) in cold CH_2Cl_2 (2 ml) was added dropwise and the reaction mixture was stirred for 10 min at 0 °C and then for 30 min at room

temperature. Upon completion of the reaction, the mixture was treated according to the general procedure to yield product **7** quantitatively. ^{1}H NMR ($CDCl_3$, 600 MHz), δ/ppm: 2.99 (s, 3H), 2.21-2.18 (m, 6H), 2.03 (br. s, 3H), 1.78 (br. s, 3H), 1.74-1.68 (m, 7H). ^{13}C NMR ($CDCl_3$, 150 MHz), δ/ppm: 91.5 (1C), 43.2 (3C), 40.9 (1C), 40.2 (3C), 36.7 (3C), 35.9 (3C), 25.2 (1C). MS (EI), *m*/*z*: 204.2 (M^+–CH_3O_2S+H). HRMS (MALDI): calcd. for $[C_{15}H_{22}O_3SNa]^+$ 305.1187; found 305.1180.

Computations: The semi-empirical quantum mechanical GFN2-xTB method[65, 66] was used for geometry optimization of ether molecules on the graphite surface consisting of two layers of 400 carbon atoms in total. Initial geometry optimization of ether molecules was performed with the Orca 5 program package[75, 76] using the B3LYP-D3(BJ)/def2-TZVPP level of theory[77-82] and the obtained minima were verified by frequency computations. The same level of theory was used for obtaining electron density distribution of the optimized on-surface ether assemblies. NCI plots were obtained using Multiwfn 3.6[83] and visualized by VMD software.[84] Simulated STM plots were generated from density cube files using the critic2 program.[85, 86]

HOPG monolayer formation and STM measurements: A droplet of a saturated solution of the corresponding diamondoid ether (**1**–**4**) in octan-1-ol was deposited on the freshly cleaved HOPG substrate (Bruker). STM measurements were performed at the liquid/solid interface on a MultiMode8 (Bruker) instrument by using commercially available Pt/Ir tips (Bruker, 0.25 mm diameter). All measurements were performed in the constant-height mode under ambient conditions and humidity of 40–50%. Tunneling currents were in the range from 0.05 to 1 nA, and the bias voltage in the range from 0.5 to 1 V. STM images were processed and analyzed by using the NanoScope Analysis 2.0 (Bruker) software.

X-ray crystallography methods: Crystallizations were performed by slow evaporation of the solvents (**1** from pentane, **2** from hexane, **3** from dioxane, and **4** from hexane). Crystals were mounted on a glass fiber and then fixed to the goniometer head of the X-ray diffractometer. The data on single crystals of compounds **1**–**4** were collected on a Xcalibur Nova single crystal diffractometer equipped with Ruby CCD detector, using Cu Kα X-ray radiation with wavelength of λ = 1.5412 Å. The crystals were kept at room temperature during data collection, except compound **2** which was kept at 160 K. Using Olex2,[87] the structures were solved with the ShelXT[88] structure solution program using Intrinsic Phasing and refined with the ShelXL[88] refinement package using Least Squares minimization. Hydrogen atoms in these structures were introduced at calculated positions and treated using appropriate riding models. All non-hydrogen atoms were refined anisotropically. Crystal structures reported

herein were deposited in the CSD and were allocated the following CCDC deposition numbers: 2156453 (**1**), 2156485 (**2**), 2156514 (**3**) and 2156490 (**4**). These data contain the supplementary crystallographic information for this paper and can be obtained free of charge from the Cambridge Crystallographic Data Centre *via* www.ccdc.cam.ac.uk/data_request/cif.

Supporting Information

Supporting Information contains details on synthesis, STM measurements, X-ray crystallography methods and computations.

AUTHOR INFORMATION

Corresponding Authors

*E-mail: msekutor@irb.hr

*E-mail: ibiljan@chem.pmf.hr

ORCID

J. Alić: 0000-0002-8289-5826

Ivana Biljan: 0000-0002-0650-1063

Zoran Štefanić: 0000-0002-3486-4291

M. Šekutor: 0000-0003-1629-3672

Author Contributions

The manuscript was written through contributions of all authors. All authors have given approval to the final version of the manuscript.

Notes

The authors declare no competing financial interest.

Data availability statement

The data that support the findings of this study are available upon request from the authors.

Acknowledgements

These materials are based on work financed by the Croatian Science Foundation (HRZZ, UIP-2017-05-9653). The support of infrastructural project CIuK co-financed by the Croatian

Government and the European Union through the European Regional Development Fund - Competitiveness and Cohesion Operational Programme (grant number KK.01.1.1.02.0016) is acknowledged. The authors thank Dr. Krunoslav Užarević and Mr. Tomislav Stolar for the determination of melting points. The computations were performed on the HPC Isabella based in SRCE–University of Zagreb, University Computing Centre for computational resources.

References

[1] Reina G, Zhao L, Bianco A and Komatsu N 2019 Chemical Functionalization of Nanodiamonds: Opportunities and Challenges Ahead *Angew. Chem. Int. Ed.* **58** 17918–29

[2] Schwertfeger H, Fokin A A and Schreiner P R 2008 Diamonds are a Chemist's Best Friend: Diamondoid Chemistry Beyond Adamantane *Angew. Chem. Int. Ed.* **47** 1022–36

[3] Gunawan M A, Hierso J-C, Poinsot D, Fokin A A, Fokina N A, Tkachenko B A and Schreiner P R 2014 Diamondoids: functionalization and subsequent applications of perfectly defined molecular cage hydrocarbons *New J. Chem.* **38** 28–41

[4] Dahl J E, Liu S G and Carlson R M K 2003 Isolation and Structure of Higher Diamondoids, Nanometer-Sized Diamond Molecules *Science* **299** 96–9

[5] Fokina N A, Tkachenko B A, Merz A, Serafin M, Dahl J E P, Carlson R M K, Fokin A A and Schreiner P R 2007 Hydroxy Derivatives of Diamantane, Triamantane, and [121]Tetramantane: Selective Preparation of Bis-Apical Derivatives *Eur. J. Org. Chem.* **2007** 4738–45

[6] Fokin A A and Schreiner P R 2012 *Strategies and Tactics in Organic Synthesis,* ed M Harmata: Academic Press) p 317–50

[7] Clay W A, Liu Z, Yang W, Fabbri J D, Dahl J E, Carlson R M K, Sun Y, Schreiner P R, Fokin A A, Tkachenko B A, Fokina N A, Pianetta P A, Melosh N and Shen Z-X 2009 Origin of the Monochromatic Photoemission Peak in Diamondoid Monolayers *Nano Lett.* **9** 57–61

[8] Yang W L, Fabbri J D, Willey T M, Lee J R I, Dahl J E, Carlson R M K, Schreiner P R, Fokin A A, Tkachenko B A, Fokina N A, Meevasana W, Mannella N, Tanaka K, Zhou X J, van Buuren T, Kelly M A, Hussain Z, Melosh N A and Shen Z-X 2007 Monochromatic Electron Photoemission from Diamondoid Monolayers *Science* **316** 1460–2

[9] Roth S, Leuenberger D, Osterwalder J, Dahl J E, Carlson R M K, Tkachenko B A, Fokin A A, Schreiner P R and Hengsberger M 2010 Negative-electron-affinity diamondoid monolayers as high-brilliance source for ultrashort electron pulses *Chem. Phys. Lett.* **495** 102–8

[10] Held P A, Fuchs H and Studer A 2017 Covalent-Bond Formation via On-Surface Chemistry *Chem. Eur. J.* **23** 5874–92

[11] Pavliček N and Gross L 2017 Generation, manipulation and characterization of molecules by atomic force microscopy *Nat. Rev. Chem.* **1** 0005

[12] Cui D, MacLeod J M and Rosei F 2018 Probing functional self-assembled molecular architectures with solution/solid scanning tunnelling microscopy *Chem. Commun.* **54** 10527–39

[13] Ding Y, Wang X, Xie L, Yao X and Xu W 2018 Two-dimensional self-assembled nanostructures of nucleobases and their related derivatives on Au(111) *Chem. Commun.* **54** 9259–69

[14] Goronzy D P, Ebrahimi M, Rosei F, Arramel, Fang Y, De Feyter S, Tait S L, Wang C, Beton P H, Wee A T S, Weiss P S and Perepichka D F 2018 Supramolecular Assemblies on Surfaces: Nanopatterning, Functionality, and Reactivity *ACS Nano* **12** 7445–81

[15] Gross L, Schuler B, Pavliček N, Fatayer S, Majzik Z, Moll N, Peña D and Meyer G 2018 Atomic Force Microscopy for Molecular Structure Elucidation *Angew. Chem. Int. Ed.* **57** 3888–908

[16] Xing L, Peng Z, Li W and Wu K 2019 On Controllability and Applicability of Surface Molecular Self-Assemblies *Acc. Chem. Res.* **52** 1048–58

[17] Cai Z, Liu M, She L, Li X, Lee J, Yao D-X, Zhang H, Chi L, Fuchs H and Zhong D 2015 Linear Alkane C–C Bond Chemistry Mediated by Metal Surfaces *ChemPhysChem* **16** 1356–60
[18] Cai L, Sun Q, Zhang C, Ding Y and Xu W 2016 Dehydrogenative Homocoupling of Alkyl Chains on Cu(110) *Chem. Eur. J.* **22** 1918–21
[19] Hu Y, Miao K, Zha B, Xu L, Miao X and Deng W 2016 STM investigation of structural isomers: alkyl chain position induced self-assembly at the liquid/solid interface *Phys. Chem. Chem. Phys.* **18** 624–34
[20] Yang B, Lin H, Miao K, Zhu P, Liang L, Sun K, Zhang H, Fan J, Meunier V, Li Y, Li Q and Chi L 2016 Catalytic Dealkylation of Ethers to Alcohols on Metal Surfaces *Angew. Chem. Int. Ed.* **55** 9881–5
[21] Zhang J, Chang C-r, Yang B, Cao N, Peng C, Zhang H, Tang D-T D, Glorius F, Erker G, Fuchs H, Li Q and Chi L 2017 Step-Edge Assisted Direct Linear Alkane Coupling *Chem. Eur. J.* **23** 6185–9
[22] Fang Y, Cibian M, Hanan G S, Perepichka D F, De Feyter S, Cuccia L A and Ivasenko O 2018 Alkyl chain length effects on double-deck assembly at a liquid/solid interface *Nanoscale* **10** 14993–5002
[23] Schuler B, Zhang Y, Collazos S, Fatayer S, Meyer G, Pérez D, Guitián E, Harper M R, Kushnerick J D, Peña D and Gross L 2017 Characterizing aliphatic moieties in hydrocarbons with atomic force microscopy *Chem. Sci.* **8** 2315–20
[24] Sakai Y, Nguyen G D, Capaz R B, Coh S, Pechenezhskiy I V, Hong X, Wang F, Crommie M F, Saito S, Louie S G and Cohen M L 2013 Intermolecular interactions and substrate effects for an adamantane monolayer on a Au(111) surface *Phys. Rev, B* **88** 235407
[25] Wang Y, Kioupakis E, Lu X, Wegner D, Yamachika R, Dahl J E, Carlson R M K, Louie S G and Crommie M F 2008 Spatially resolved electronic and vibronic properties of single diamondoid molecules *Nat. Mater.* **7** 38–42
[26] Pechenezhskiy I V, Hong X, Nguyen G D, Dahl J E P, Carlson R M K, Wang F and Crommie M F 2013 Infrared Spectroscopy of Molecular Submonolayers on Surfaces by Infrared Scanning Tunneling Microscopy: Tetramantane on Au(111) *Phys. Rev. Lett.* **111** 126101
[27] Ebeling D, Šekutor M, Stiefermann M, Tschakert J, Dahl J E P, Carlson R M K, Schirmeisen A and Schreiner P R 2017 London Dispersion Directs On-Surface Self-Assembly of [121]Tetramantane Molecules *ACS Nano* **11** 9459–66
[28] Ebeling D, Šekutor M, Stiefermann M, Tschakert J, Dahl J E P, Carlson R M K, Schirmeisen A and Schreiner P R 2018 Assigning the absolute configuration of single aliphatic molecules by visual inspection *Nat. Commun.* **9** 2420
[29] Lopatina Y Y, Vorobyova V I, Fokin A A, Schreiner P R, Marchenko A A and Zhuk T S 2019 Structures and Dynamics in Thiolated Diamantane Derivative Monolayers *J. Phys. Chem. C* **123** 27477–82
[30] Feng K, Solel E, Schreiner P R, Fuchs H and Gao H-Y 2021 Diamantanethiols on Metal Surfaces: Spatial Configurations, Bond Dissociations, and Polymerization *J. Phys. Chem. Lett.* **12** 3468–75
[31] Willey T M, Lee J R I, Fabbri J D, Wang D, Nielsen M H, Randel J C, Schreiner P R, Fokin A A, Tkachenko B A, Fokina N A, Dahl J E P, Carlson R M K, Terminello L J, Melosh N A and van Buuren T 2009 Determining orientational structure of diamondoid thiols attached to silver using near-edge X-ray absorption fine structure spectroscopy *J. Electron Spectrosc. Relat. Phenom.* **172** 69–77
[32] Voros M, Demjen T, Szilvasi T and Gali A 2012 Tuning the optical gap of nanometer-size diamond cages by sulfurization: a time-dependent density functional study *Phys. Rev. Lett.* **108** 267401/1–/5
[33] Richter R, Wolter D, Zimmermann T, Landt L, Knecht A, Heidrich C, Merli A, Dopfer O, Reiss P, Ehresmann A, Petersen J, Dahl J E, Carlson R M K, Bostedt C, Moeller T, Mitric R and Rander T 2014 Size and shape dependent photoluminescence and excited state decay rates of diamondoids *Phys. Chem. Chem. Phys.* **16** 3070–6

[34] Richter R, Roehr M I S, Zimmermann T, Petersen J, Heidrich C, Rahner R, Moeller T, Dahl J E, Carlson R M K, Mitric R, Rander T and Merli A 2015 Laser-induced fluorescence of free diamondoid molecules *Phys. Chem. Chem. Phys.* **17** 4739–49
[35] Narasimha K T, Ge C, Fabbri J D, Clay W, Tkachenko B A, Fokin A A, Schreiner P R, Dahl J E, Carlson R M K, Shen Z X and Melosh N A 2016 Ultralow effective work function surfaces using diamondoid monolayers *Nat. Nanotechnol.* **11** 267–72
[36] Fokin A A and Schreiner P R 2009 Band gap tuning in nanodiamonds: first principle computational studies *Mol. Phys.* **107** 823–30
[37] Fokin A A, Zhuk T S, Pashenko A E, Dral P O, Gunchenko P A, Dahl J E P, Carlson R M K, Koso T V, Serafin M and Schreiner P R 2009 Oxygen-Doped Nanodiamonds: Synthesis and Functionalizations *Org. Lett.* **11** 3068–71
[38] Fokin A A, Zhuk T S, Blomeyer S, Pérez C, Chernish L V, Pashenko A E, Antony J, Vishnevskiy Y V, Berger R J F, Grimme S, Logemann C, Schnell M, Mitzel N W and Schreiner P R 2017 Intramolecular London Dispersion Interaction Effects on Gas-Phase and Solid-State Structures of Diamondoid Dimers *J. Am. Chem. Soc.* **139** 16696–707
[39] Kraatz U 1973 Synthesis of 1-adamantyl aryl ethers *Chem. Ber.* **106** 3095–6
[40] Lloris M E, Marquet J and Moreno-Manas M 1990 Alkylations of α-methyl-substituted β-diketones through their copper(II) complexes. Preparation of sterically congested β-diketones *Tetrahedron Lett.* **31** 7489–92
[41] Lloris M E, Galvez N, Marquet J and Moreno-Manas M 1991 Reactions of copper(II) β-diketonates under free radical conditions. Preparation of highly congested β-diketones *Tetrahedron* **47** 8031–42
[42] Tsypin V G, Pevzner M S and Golod E L 2001 Oxidative alkylation of azoles: VII. Adamantylation of azoles via oxidative generation of 1-adamantyl cations *Russ. J. Org. Chem.* **37** 1762–6
[43] Creary X, Willis E D and Gagnon M 2005 Carbocation-Forming Reactions in Ionic Liquids *J. Am. Chem. Soc.* **127** 18114–20
[44] Lohr T L, Li Z, Assary R S, Curtiss L A and Marks T J 2015 Thermodynamically Leveraged Tandem Catalysis for Ester RC(O)O–R′ Bond Hydrogenolysis. Scope and Mechanism *ACS Catal.* **5** 3675–9
[45] Quesada Moreno M M, Pinacho P, Pérez C, Šekutor M, Schreiner P R and Schnell M 2020 London Dispersion and Hydrogen-Bonding Interactions in Bulky Molecules: The Case of Diadamantyl Ether Complexes *Chem. Eur. J.* **26** 10817–25
[46] Wagner J P and Schreiner P R 2015 London Dispersion in Molecular Chemistry-Reconsidering Steric Effects *Angew. Chem. Int. Ed.* **54** 12274–96
[47] Quesada-Moreno M M, Pinacho P, Pérez C, Šekutor M, Schreiner P R and Schnell M 2021 Do Docking Sites Persist Upon Fluorination? The Diadamantyl Ether-Aromatics Challenge for Rotational Spectroscopy and Theory *Chem. Eur. J.* **27** 6198–203
[48] Crossland R K and Servis K L 1970 Facile synthesis of methanesulfonate esters *J. Org. Chem.* **35** 3195–6
[49] De Feyter S, Gesquière A, Abdel-Mottaleb M M, Grim P C M, De Schryver F C, Meiners C, Sieffert M, Valiyaveettil S and Müllen K 2000 Scanning Tunneling Microscopy: A Unique Tool in the Study of Chirality, Dynamics, and Reactivity in Physisorbed Organic Monolayers *Acc. Chem. Res.* **33** 520–31
[50] De Feyter S and De Schryver F C 2005 Self-Assembly at the Liquid/Solid Interface: STM Reveals *J. Phys. Chem. B* **109** 4290–302
[51] Wang L, Chen Q, Pan G-B, Wan L-J, Zhang S, Zhan X, Northrop B H and Stang P J 2008 Nanopatterning of Donor/Acceptor Hybrid Supramolecular Architectures on Highly Oriented Pyrolytic Graphite: A Scanning Tunneling Microscopy Study *J. Am. Chem. Soc.* **130** 13433–41
[52] Zha B, Li J, Wu J, Miao X and Zhang M 2019 Cooperation and competition of hydrogen and halogen bonds in 2D self-assembled nanostructures based on bromine substituted coumarins *New J. Chem.* **43** 17182–7

[53] Li J, Zu X, Qian Y, Duan W, Xiao X and Zeng Q 2020 Advances in self-assembly and regulation of aromatic carboxylic acid derivatives at HOPG interface *Chin. Chem. Lett.* **31** 10–8
[54] Peng X, Zhao F, Peng Y, Li J and Zeng Q 2020 Dynamic surface-assisted assembly behaviours mediated by external stimuli *Soft Matter* **16** 54–63
[55] Ma C, Li J, Zhang S, Duan W and Zeng Q 2021 Progress in self-assemblies of macrocycles at the liquid/solid interface *Nanotechnology* **32** 382001
[56] Bléger D, Kreher D, Mathevet F, Attias A-J, Schull G, Huard A, Douillard L, Fiorini-Debuischert C and Charra F 2007 Surface Noncovalent Bonding for Rational Design of Hierarchical Molecular Self-Assemblies *Angew. Chem. Int. Ed.* **46** 7404–7
[57] Chen Q, Yan H-J, Yan C-J, Pan G-B, Wan L-J, Wen G-Y and Zhang D-Q 2008 STM investigation of the dependence of alkane and alkane (C18H38, C19H40) derivatives self-assembly on molecular chemical structure on HOPG surface *Surf Sci.* **602** 1256–66
[58] Chen Q, Chen T, Zhang X, Wan L-J, Liu H-B, Li Y-L and Stang P 2009 Two-dimensional OPV4 self-assembly and its coadsorption with alkyl bromide: from helix to lamellar *Chem. Commun.* 3765–7
[59] Krukowski P, Klusek Z, Olejniczak W, Klepaczko R, Puchalski M, Dabrowski P, Kowalczyk P J and Gwozdzinski K 2009 Self-assembled monolayers of radical molecules physisorbed on HOPG(0001) substrate studied by scanning tunnelling microscopy and electron paramagnetic resonance techniques *Appl. Surf. Sci.* **255** 8769–73
[60] Arrigoni C, Schull G, Bléger D, Douillard L, Fiorini-Debuisschert C, Mathevet F, Kreher D, Attias A-J and Charra F 2010 Structure and Epitaxial Registry on Graphite of a Series of Nanoporous Self-Assembled Molecular Monolayers *J. Phys. Chem. Lett.* **1** 190–4
[61] Miao X, Chen C, Zhou J and Deng W 2010 Influence of hydrogen bonds and double bonds on the alkane and alkene derivatives self-assembled monolayers on HOPG surface: STM observation and computer simulation *Appl. Surf. Sci.* **256** 4647–55
[62] Miao X, Xu L, Liao C, Li Z, Zhou J and Deng W 2011 Two-dimensional self-assembly of esters with different configurations at the liquid–solid interface *Appl. Surf. Sci.* **257** 4559–65
[63] Guo C, Xue J D, Cheng L X, Liu R C, Kang S Z, Zeng Q D and Li M 2017 Two-dimensional self-assembly of diacetylenic acid derivatives and their light-induced polymerization on HOPG surfaces *Phys. Chem. Chem. Phys.* **19** 16213–8
[64] Berrocal J A, Heideman G H, de Waal B F M, Enache M, Havenith R W A, Stöhr M, Meijer E W and Feringa B L 2020 Engineering Long-Range Order in Supramolecular Assemblies on Surfaces: The Paramount Role of Internal Double Bonds in Discrete Long-Chain Naphthalenediimides *J. Am. Chem. Soc.* **142** 4070–8
[65] Grimme S, Bannwarth C and Shushkov P 2017 A Robust and Accurate Tight-Binding Quantum Chemical Method for Structures, Vibrational Frequencies, and Noncovalent Interactions of Large Molecular Systems Parametrized for All spd-Block Elements (Z = 1-86) *J. Chem. Theory Comput.* **13** 1989–2009
[66] Bannwarth C, Ehlert S and Grimme S 2019 GFN2-xTB-An Accurate and Broadly Parametrized Self-Consistent Tight-Binding Quantum Chemical Method with Multipole Electrostatics and Density-Dependent Dispersion Contributions *J. Chem. Theory Comput.* **15** 1652–71
[67] Gao H-Y, Šekutor M, Liu L, Timmer A, Schreyer H, Mönig H, Amirjalayer S, Fokina N A, Studer A, Schreiner P R and Fuchs H 2019 Diamantane Suspended Single Copper Atoms *J. Am. Chem. Soc.* **141** 315–22
[68] Grimme S, Antony J, Ehrlich S and Krieg H 2010 A consistent and accurate ab initio parametrization of density functional dispersion correction (DFT-D) for the 94 elements H-Pu *J. Chem. Phys.* **132** 154104
[69] Grimme S 2011 Density functional theory with London dispersion corrections *WIREs Comput. Mol. Sci.* **1** 211–28
[70] Grimme S, Ehrlich S and Goerigk L 2011 Effect of the damping function in dispersion corrected density functional theory *J. Comput. Chem.* **32** 1456–65

[71] Wagner J P and Schreiner P R 2014 Nature Utilizes Unusual High London Dispersion Interactions for Compact Membranes Composed of Molecular Ladders *J. Chem. Theory Comput.* **10** 1353–8
[72] Wang C, Mo Y, Wagner J P, Schreiner P R, Jemmis E D, Danovich D and Shaik S 2015 The Self-Association of Graphane Is Driven by London Dispersion and Enhanced Orbital Interactions *J. Chem. Theory Comput.* **11** 1621–30
[73] Rochefort A and Wuest J D 2009 Interaction of Substituted Aromatic Compounds with Graphene *Langmuir* **25** 210–5
[74] Kevill D N, Kolwyck K C and Weitl F L 1970 Correlation of solvolysis rates of 1-adamantyl p-toluenesulfonate *J. Am. Chem. Soc.* **92** 7300–6
[75] Neese F 2012 The ORCA program system *WIREs Comput. Mol. Sci.* **2** 73–8
[76] Neese F 2018 Software update: the ORCA program system, version 4.0 *WIREs Comput. Mol. Sci.* **8** e1327
[77] Becke A D 1993 Density-functional thermochemistry. III. The role of exact exchange *J. Chem. Phys.* **98** 5648–52
[78] Lee C, Yang W and Parr R G 1988 Development of the Colle-Salvetti correlation-energy formula into a functional of the electron density *Phys. Rev, B* **37** 785–9
[79] Grimme S, Antony J, Ehrlich S and Krieg H 2010 A consistent and accurate ab initio parametrization of density functional dispersion correction (DFT-D) for the 94 elements H-Pu *J. Chem. Phys.* **132** 154104
[80] Grimme S, Ehrlich S and Goerigk L 2011 Effect of the damping function in dispersion corrected density functional theory *J. Comput. Chem.* **32** 1456–65
[81] Weigend F and Ahlrichs R 2005 Balanced basis sets of split valence, triple zeta valence and quadruple zeta valence quality for H to Rn: Design and assessment of accuracy *Phys. Chem. Chem. Phys.* **7** 3297–305
[82] Weigend F 2006 Accurate Coulomb-fitting basis sets for H to Rn *Phys. Chem. Chem. Phys.* **8** 1057–65
[83] Lu T and Chen F 2012 Multiwfn: A multifunctional wavefunction analyzer *J. Comput. Chem.* **33** 580–92
[84] Humphrey W, Dalke A and Schulten K 1996 VMD: Visual molecular dynamics *J. Mol. Graphics* **14** 33–8
[85] Otero-de-la-Roza A, Blanco M A, Pendás A M and Luaña V 2009 Critic: a new program for the topological analysis of solid-state electron densities *Comput. Phys. Commun.* **180** 157–66
[86] Otero-de-la-Roza A, Johnson E R and Luaña V 2014 Critic2: A program for real-space analysis of quantum chemical interactions in solids *Comput. Phys. Commun.* **185** 1007–18
[87] Dolomanov O V, Bourhis L J, Gildea R J, Howard J A K and Puschmann H 2009 OLEX2: a complete structure solution, refinement and analysis program *J. Appl. Crystallogr.* **42** 339–41
[88] Sheldrick G 2015 SHELXT - Integrated space-group and crystal-structure determination *Acta Crystallogr., Sect. A* **71** 3–8